Research Square

Preprints are preliminary reports that have not undergone peer review.
They should not be considered conclusive, used to inform clinical practice,
or referenced by the media as validated information.

Multi-omics of C9orf72 spinal cord organoids reveal convergent molecular signatures and targets

Mafalda Rizzuti
Fondazione IRCCS Ca' Granda Ospedale Maggiore Policlinico
Noemi Galli
Fondazione IRCCS Ca' Granda Ospedale Maggiore Policlinico
Giorgia Galvani
Fondazione IRCCS Ca' Granda Ospedale Maggiore Policlinico
Lorenzo Brambilla
Fondazione IRCCS Ca' Granda Ospedale Maggiore Policlinico
Michela Ripolone
Fondazione IRCCS Ca' Granda Ospedale Maggiore Policlinico
Laura Napoli
Fondazione IRCCS Ca' Granda Ospedale Maggiore Policlinico
Enrico Sebastiani
Fondazione IRCCS Ca' Granda Ospedale Maggiore Policlinico
Akihiro Maeda
Fondazione IRCCS Ca' Granda Ospedale Maggiore Policlinico
Niccolò Bolli
Fondazione IRCCS Ca' Granda Ospedale Maggiore Policlinico
Roberto Del Bo
University of Milan
Udit Sheth
Mayo Clinic
Tanya Gendron
Mayo Clinic
Jeroen Pasterkamp
University Medical Center Utrecht
Linda Ottoboni
University of Milan
Stefania Corti
stefania.corti@unimi.it

University of Milan

Research Article

Keywords: C9orf72, ALS, organoids, spinal cord organoids, multi-omics, therapeutic targets

Posted Date: July 8th, 2026

DOI: https://doi.org/10.21203/rs.3.rs-10053820/v1

License: This work is licensed under a Creative Commons Attribution 4.0 International License.
Read Full License

Additional Declarations: No competing interests reported.

Abstract

Background: amyotrophic lateral sclerosis is the most common adult-onset motor neuron disease, characterised by the progressive degeneration of upper and lower motor neurons in the brain and spinal cord. Despite substantial advances in the understanding of underlying disease mechanisms, effective therapies remain lacking.

Methods: we generated spinal cord organoids from patient-derived induced pluripotent stem cells and matched isogenic controls to model *in vitro* the molecular pathology associated with the hexanucleotide repeat expansion within the *C9orf72* gene.

Results: C9orf72 organoids displayed delayed neuronal maturation, axonal degeneration, mitochondrial abnormalities, enhanced apoptotic signaling, and accumulation of dipeptide repeat proteins. Integrated multi-omics analyses revealed a consistent down-regulation of Netrin-1 at both the transcript and protein levels across patient-derived organoids, suggesting that its loss may contribute to impaired neuronal connectivity, compromised axonal integrity, and increased motor neuron vulnerability in C9orf72 amyotrophic lateral sclerosis.

Conclusions: together, these findings establish patient-derived spinal cord organoids as a biologically relevant and *in vitro* model that recapitulates key cellular and molecular hallmarks of C9orf72-associated amyotrophic lateral sclerosis. This platform provides a valuable framework to deepen disease mechanisms, toward the development of new effective therapeutic strategies.

Background

Amyotrophic Lateral Sclerosis (ALS) is the most prevalent adult-onset motor neuron disease (MND), characterised by progressive degeneration of upper and lower motor neurons (MNs) in the brain and spinal cord. This neuronal loss leads to muscle weakness, atrophy, and spasticity, ultimately resulting in respiratory failure and death, typically within 2–5 years of diagnosis (1–3). Despite numerous clinical trials, approved treatments provide only modest survival benefits, highlighting the urgent need for improved disease models and therapeutic strategies.

Approximately 10–15% of ALS cases are familial (fALS) with Mendelian inheritance, whereas the remaining 85–90% are sporadic (sALS) without clear familial history (4). Multiple causative genes have been linked to both forms (5). Among the more than 40 identified ALS genes, hexanucleotide repeat expansions (HREs) in *chromosome 9 open reading frame 72* (*C9orf72*) represent the most common genetic cause, accounting for ~ 40% of familial and ~ 8% of sporadic cases, as well as a significant proportion of frontotemporal dementia (FTD) cases. The pathological HRE drives three interconnected, non-mutually exclusive mechanisms involving both loss-of-function and toxic gain-of-function effects (6,7). Indeed, the HRE is transcribed bidirectionally into repetitive RNA, which accumulates in sense and antisense foci (8). Furthermore, these RNAs undergo non-canonical repeat-associated non-ATG (RAN) translation, generating aggregating dipeptide repeat proteins (DPRs) (9,10).

Although its precise function remains incompletely understood, C9orf72 has been implicated in diverse cellular processes, including vesicle trafficking, lysosome homeostasis, autophagy, stress granule dynamics, lipid metabolism, axon growth and transport (11–16).

Three-dimensional (3D) organoid models offer a powerful approach to recapitulate tissue architecture and cell-cell interactions more faithfully than traditional 2D cultures, which is particularly relevant for multifactorial diseases such as ALS. Concurrently, advances in omics technologies now enable the collection and integration of high-throughput datasets spanning genomics, transcriptomics, proteomics, and metabolomics (5,17). Such multi-omics integration can yield comprehensive molecular profiles, enabling the identification of disease subtypes and molecular signatures, elucidation of regulatory pathways, and improved prediction of therapeutic responses (18,19).

In this study, spinal cord organoids (SCOs) were generated from induced pluripotent stem cells (iPSC) lines carrying the *C9orf72* HRE and paired isogenic controls. A combined approach by integrating transcriptomic and proteomic analyses enabled the identification of dysregulated pathways and potential therapeutic targets with translational relevance, paving the way for the development of more effective, mechanism-based treatment strategies.

Material & Methods

Ethical approval

iPSC line #1 carrying the *C9orf72* expansion and its paired isogenic control were obtained from Siddharthan Chandran's Laboratory under full Ethical and Institutional Review Board approval from the University of Edinburgh (20). iPSC lines #2 and #3 were obtained from the Cedars-Sinai Medical Centre iPSC Core Facility in Los Angeles, USA.

iPSC maintenance and quality control

All iPSCs and paired isogenic lines were generated using CRISPR/Cas9 technology and grown in Essential 8™ medium (Thermo Fisher Scientific) on Matrigel-coated plates (Cultrex Basement Membrane Extract, Corning Life Science). Cells were regularly tested for mycoplasma contamination using the MycoAlert® Mycoplasma Detection Kit (Lonza). All lines underwent karyotype analysis to screen for chromosomal aberrations.

C9orf72 repeat expansion analysis

HRE presence was confirmed in all iPSC lines using Repeat-Primed PCR with the AmplideX® PCR/CE *C9orf72* Kit (Bio-techne, Asuragen). PCR products were analysed on a 3100 DNA Analyzer (Applied

Biosystems) with the GeneScan™ 500 LIZ® size standard (Applied Biosystems). Fragment analysis was performed using GeneMapper software (Applied Biosystems).

Generation of iPSC-derived SCOs

SCOs were generated as previously described (21). Briefly, at 0 days *in vitro* (DIV), iPSCs were detached, counted, and grown in suspension in low-attachment 96-well plates containing human Embryonic Stem (hES) medium supplemented with FGF2 and Y-27632 ROCK Inhibitor to induce embryoid body (EB) formation. EBs were maintained in hES medium supplemented with SB431642, CHIR99021, and LDN193189 to promote neuroectodermal differentiation until DIV6, when they were transferred to low-attachment 24-well plates. Organoids were grown in Neural induction medium (NIM) supplemented with the same small molecules plus Retinoic Acid (RA) for caudalisation. At DIV12, EBs were embedded in Matrigel (Cultrex® stem cell qualified reduced growth factor basement membrane extract) droplets and cultured in medium containing RA and Smoothened agonist (SAG) for ventral patterning for 2 days before transfer to spinning bioreactors. From DIV28, medium was supplemented with BDNF, GDNF, and IGF-II to promote neuronal maturation. Organoids were maintained at 37°C with 5% CO_2 until DIV80.

Immunofluorescence (IF) and quantification

SCOs were fixed in 4% paraformaldehyde (PFA) for 15 minutes at 4°C, cryoprotected in 30% sucrose overnight at 4°C, and embedded in 7.5% sucrose/10% gelatin (bovine skin type B, Sigma-Aldrich). Blocks containing 3 organoids were frozen on dry ice and stored at -80°C. Sections (10-12 µm) were cut using a cryostat and blocked with 5% normal goat serum (NGS), 5% bovine serum albumin (BSA), and 0.1% Triton-X-100 in PBS for 1 hour at room temperature (RT). Sections were incubated overnight at 4°C with primary antibodies (Supplementary Table 1), followed by Alexa Fluor secondary antibodies (1:1000) for 1.5 hours at RT. Nuclei were counterstained with DAPI. Images were acquired using the LEICA SP8 confocal microscope. Quantification was performed using Fiji ImageJ with automated thresholding. A minimum of 3 sections per organoid and 4-6 random fields per section were analysed by investigators blinded to experimental conditions.

Apoptosis was assessed using the DeadEnd™ Fluorometric TUNEL system (Promega). Images were acquired with a fluorescence microscope (LEICA), and TUNEL-positive area was quantified relative to the total area of DAPI-positive cells.

Real-time PCR

RNA was extracted from organoids using the ReliaPrep™ RNA Cell Kit (Promega). Total RNA (500 ng) was reverse-transcribed using SuperScript VILO Master Mix (Thermo Fisher Scientific). Quantitative PCR (qPCR) was performed with TaqMan® Universal Master Mix and gene-specific TaqMan® Assays

(Thermo Fisher Scientific) on a 7500 Real-Time PCR System (Applied Biosystems), using *GAPDH* or *ACTIN* as reference. Data represent mean of triplicates. Only Ct values <35 were included. All assay details are provided in Supplementary Table 2.

Meso-scale discovery immunoassay (MSD)

Organoids were lysed by adding Co-IP buffer (50 mM Tris-HCl pH 7.4, 300 mM NaCl, 1% Triton, 5 mM EDTA, 1 mM phenylmethylsulfonyl fluoride (PMSF), Phosphatase Inhibitor Cocktail (Bimake, cat. #B1500), and Protease Inhibitor Cocktail (EMD Millipore, cat. #539131). Samples were homogenised by pipetting, supplemented with 2% sodium dodecyl sulfate (SDS), sonicated, and centrifuged at maximum speed at RT. Protein concentration was determined using the bicinchoninic acid (BCA) assay. MSD technology was employed to quantify poly(GA) and poly(GP) detection using an affinity purified monoclonal poly(GA) antibody (clone 5E9, Cat. #MABN889, Millipore Sigma) as both the capture antibody (5E9, 2 µg/mL), and the detection antibody (sulfo-tagged 5E9, 2 µg/mL); an affinity purified monoclonal poly(GP) antibody (TALS 828.179) generated by Target ALS was used as both the capture antibody (biotinylated TALS 828.179, 2 µg/mL), and the detection antibody (sulfo-tagged TALS 828.179, 2 µg/mL) for the poly(GP) immunoassay. Samples were diluted in Tris-buffered saline and tested in duplicate. Response values corresponding to the intensity of emitted light upon electrochemical stimulation of the assay plate using the MSD QUICKPLEX SQ120 were acquired. Positive and negative controls were tested in conjunction with the samples. Poly(GA) and poly(GP) levels are presented in arbitrary units.

Transmission Electron Microscopy (TEM)

Organoids were fixed in 2 % glutaraldehyde (pH 7.4) (Electron Microscopy Sciences EMS, Hatfield, PA, USA), for 15 minutes at room temperature and O.N. at 4 °C. The specimens were washed in 0.1 M, pH 7.4 cacodylate buffer (EMS), post-fixed for 1 hour in 1% osmium tetroxide (EMS) and dehydrated using a graded series of ethyl alcohol. Finally, ultrathin sections (80 nm thick slices) were prepared using an ultramicrotome Power Tome XL (RMC, Tucson, AZ, USA). The grids, stained with 0.5% lead citrate (EMS) and uranyl acetate replacement/methanol 1:1 (EMS), were examined with Hitachi HT7800 TEM (Hitachi, Japan).

Single-cell RNA sequencing (scRNA-seq)

DIV80 SCOs were dissociated using the Papain Dissociation Kit (Worthington Biochemical Corporation). Cell viability was assessed by 7-AAD staining and Fluorescence-Activated Cell Sorting (FACS). Samples (n=1 per cell line) were processed using the Chromium Next GEM Single Cell 3' Reagent Kit v3.1 (10x Genomics). Libraries were sequenced on a NovaSeq 6000 S4 flow cell (Illumina) with paired-end 150 bp reads, targeting ~100,000 reads per cell across ~9,000 cells per sample (Macrogen Europe). FASTQ files

were aligned to the GRCh38-2024-A reference genome using Cell Ranger (v=9.0.1, 10x Genomics). Gene count expression matrices generated from all samples were analysed with Scanpy (v=1.10.2) in Python 3.12.4 (22). Doublets were detected and removed using Scrublet (v=0.2.3), and low-quality cells were filtered based on the following criteria: (1) total UMI counts between 2000 and 50000; (2) number of detected genes between 1500 and 10000; (3) percentage of ribosomal gene expression <5%; and (4) percentage of mitochondrial gene expression <10% (Supplementary Fig. 1 A). Following quality control and filtering, a total of 22148 cells were retained for downstream analysis. The data were normalised using sc.pp.normalize_total(), log-transformed using sc.pp.log1p() and scaled using sc.pp.scale() with a maximum value of 10 (Supplementary Fig. 1 B). Due to substantial inter-sample variability, regression of technical and biological covariates was performed to mitigate batch effects. Specifically, total counts, percentage of ribosomal gene counts (pct_counts_ribo), number of genes per cell (n_genes_by_counts), percentage of mitochondrial gene counts (pct_counts_mt), and cell cycle phase (S and G2M) were regressed out. After regression, the data were rescaled (Supplementary Fig. 1 C). Batch correction and integration across samples were performed using the BBKNN algorithm (v=1.6.0), allowing for preservation of biological variability while minimising batch-specific effects (Supplementary Fig. 1 D). Clustering was conducted using the Leiden algorithm (v=0.10.2) at a resolution of 0.5 (23). Clusters were annotated into specific cell populations based on the expression of well-established marker genes. Following annotation, the function sc.tl.rank_genes_groups() with the *t*-test method was used to identify and verify the top 20 marker genes for each cluster. To assess the developmental potential of the cell populations, cytotrace2-py (v=1.1.0.3) was used to assign a potency score to each cell.

Differential gene expression (DGE) analysis

The Model-based Analysis of Single-cell Transcriptomics (MAST) framework was employed using the MAST R package (v=1.28.0). DGE analysis was primarily focused on MN and astrocyte clusters, due to their well-established relevance in ALS pathology. Additionally, a global DGE analysis was performed across all cells, irrespective of cluster identity, to enable direct comparison with proteomic data obtained from whole-organoid samples. Gene expression counts were normalised for library size and log-transformed prior to analysis. Cells were assigned to isogenic or C9-ALS conditions based on sample identifiers, and differential expression was assessed using hurdle models including condition as the main effect and cellular detection rate as a covariate. Statistical significance was evaluated using likelihood ratio tests, with multiple testing corrections applied using the Benjamini–Hochberg false discovery rate (*FDR*). Significantly differentially expressed genes were selected using a *FDR* threshold < 0.05 and an absolute log2 fold change (|*logFC*|) > 1. Up-regulated and down-regulated genes were analysed separately. Gene symbols were converted to Entrez Gene IDs using the org.Hs.eg.db annotation package (v=3.18.0). Functional enrichment analyses were performed using the clusterProfiler (v=4.10.1) framework. Gene Ontology (GO) enrichment was conducted for the Biological Process (BP) ontology and enrichment significance was evaluated using Benjamini–Hochberg multiple testing correction, with adjusted *p*-values < 0.05 considered significant. All comparisons were made between ALS vs isogenic

conditions. Significantly differentially expressed genes (DEGs) identified by MAST-based analysis across all cells were compared with significantly altered proteins from the proteomic dataset.

Mass spectrometry (MS)

Protein mixtures were extracted from DIV80-SCO samples using a lysis buffer containing 10 mL of 8 M Urea in 0.1 M Tris/HCl pH 8.5. Lysates were treated with protease inhibitors (5 µL/mL) and centrifuged at 15000 g for 30 minutes at 4°C. Supernatant was collected and assayed with Lowry assay. 50 µM Ambic was used to reach up to the final volume of 50 µL. MS analysis was conducted using isogenic control and C9-ALS samples from all three cell lines, across 2 separate experimental batches. The analysis was conducted at the institutional protein analysis facility Unitech Omics with an Orbitrap fusion thermo instrument.
For cell line #1, raw MS data were analysed using Proteome Discoverer™ version 2.5 (Thermo Fisher Scientific), utilising the Homo sapiens (sp_canonical, TaxID=9606) protein database version 2021-02-04 for peptide identification. For cell lines #2 and #3, the analysis was conducted using Homo sapiens (sp_incl_isoforms, TaxID=9606 and subtaxonomies) database version 2024-10-02. Protein abundance values obtained from all cell lines were integrated into a single dataset. To correct for batch effects, the removeBatchEffect() function from the Limma R package (v=3.58.1) was applied. Matrigel-associated proteins were filtered out to eliminate possible artifacts related to matrix components. Variance Stabilizing Normalization (VSN) was applied across the dataset to ensure comparability across samples. Differential protein expression analysis was performed using the Limma package, accounting for the presence of technical replicates. Genes corresponding to significantly up- or down-regulated proteins were mapped to Entrez Gene identifiers using the clusterProfiler R package and the human annotation database org.Hs.eg.db. GO enrichment analysis was performed for the BP category using the enrichGO() function. *P*-values were adjusted for multiple testing using the Benjamini–Hochberg method, and GO terms with adjusted $p < 0.05$ were considered significantly enriched. The selection of targets for validation analysis was guided by the overlapping results between proteomics and transcriptomics data.

Western blot (WB)

DIV80-SCO pellets were resuspended in lysis buffer and sonicated two times for 10 seconds at ~60 w, boiled for 5 minutes and centrifuged at 13200 g for 10 minutes. Supernatants were collected and Pierce™ BCA Protein Assay Kit (Thermo Fisher) was employed to assess protein concentration. Samples were loaded on a precast NuPAGE polyacrylamide 4-12% gel (Bio-Rad) in the presence of MES SDS Running Buffer and run for 40 minutes at 150v. Following electrophoresis, proteins on the gel were transferred to a Nitrocellulose membrane through a semi-dry transfer at 100v for 7 minutes. The membrane was blocked with Intercept® PBS Blocking Buffer (LI-COR) for 1 hour in agitation and then incubated overnight at 4°C with primary antibodies diluted in blocking solution (Supplementary Table 1). The day after, primary antibodies were removed with a 0.08% Tween-20–PBS washing buffer, and

secondary biotinylated antibodies (IRDYE, 1:15000 in blocking solution) were added for 1.5 hours at RT in dark conditions. Signal was detected with Odyssey CLx near-infrared fluorescence imaging system, and quantification was performed with LI-COR Image Studio™ software. Densitometry of the bands was performed to calculate the area under the curve. All the intensity signals referred to specific proteins were normalised to the intensity signals of selected housekeeping proteins (GAPDH or α-Tubulin).

Statistical analysis

All the obtained data were analysed using GraphPad Prism® 10. Unpaired Student's *t*-test was employed to compare two groups of data, while One-way ANOVA was used to make a comparison between three or more groups. Null hypothesis was rejected when *p* value (*p*) was < 0.05. Data are represented at mean ± standard error of the mean (SEM).

Results

iPSC-derived SCOs exhibit developmental delay and ALS-associated molecular features

All iPSC lines underwent quality control for morphology, expression of pluripotency markers, presence of the *C9orf72* HRE, and absence of mycoplasma contamination (Supplementary Fig.2 A,B). SCOs were derived from *C9orf72*-mutant iPSC lines and their respective isogenic controls (n=3/condition). All iPSC line characteristics are summarised in Table 1. One batch per cell line was generated and characterised longitudinally by brightfield imaging, IF, and qPCR at DIV30, DIV55, and DIV80 (Figure 1 A).

Table 1 Characteristics of iPSC lines. The table summarises the ID, name of the cell line, source/origin, gender, age at disease onset, and repeat expansion of C9-ALS and edited isogenic control iPSC lines employed for SCO generation.

ID	Cell line	Source/Origin	Gender	Age of onset (Y)	Repeat expansion
#1 C9-ALS	M211R2	Chandran Lab	M	52	~960 repeats
#1 isogenic	M211R2	Chandran Lab	M	52	CRISPR/Cas9 correction
#2 C9-ALS	CS29iALS-C9n1	Cedars-Sinai	M	46	c.-45+163GGGGCC[>24]
#2 isogenic	CS29iALS-C9n1	Cedars-Sinai	M	46	CRISPR/Cas9 correction
#3 C9-ALS	CS52iALS-C9n6	Cedars-Sinai	M	47	c.-45+163GGGGCC[>24]
#3 isogenic	CS52iALS-C9n6	Cedars-Sinai	M	47	CRISPR/Cas9 correction

Analysis of *Paired box 6 (PAX6)*, *Microtubule Associated Protein 2 (MAP2)*, *Choline O-acetyltransferase (ChAT)*, and *Neurofilament Heavy Chain (NEFH)* expression level over time, revealed a sustained expression of early neuroectodermal markers in both isogenic and C9-ALS organoids at DIV55, and a progressive maturation toward MN fate at day 80 (Figure 1 B). IF experiments demonstrated progressive organoid maturation at the protein level, as evidenced by the down-regulation of stemness and progenitor markers such as SRY-Box Transcription factor 2 (SOX2), ISL LIM Homeobox 1 (ISL1), and the concomitant up-regulation of late neuronal markers such as Tubulin Beta 3 Class III (TUJ1), and SMI32 (specific monoclonal antibody for non-phosphorylated neurofilament heavy and medium proteins) over time (Figure 1 C,D). Despite an increasing trend and being equally expressed in isogenic and C9-ALS organoids at DIV80, a significant difference in TUJ1 levels was observed at DIV30 and DIV55, supporting potential delayed maturation in C9-ALS samples. Notably, SMI32 levels were significantly lower in the C9-ALS cohort at all time points, especially at DIV55 and DIV80.

To further characterise organoid composition, additional IF analyses were performed for Doublecortin (DCX), MAP2, PAX6, Oligodendrocyte Transcription Factor 2 (OLIG2), Homeobox B4 (HOXB4), Peripherin (PRPH), Glial Fibrillary Acidic Protein (GFAP), and GABA. The detection of these markers, spanning neuronal progenitors, mature neurons, glial cells, and spinal cord-specific populations, confirms that by DIV80, the organoids acquired a complex and regionally relevant cellular architecture (Figure 2 A). In addition, TUNEL assay was performed to directly evaluate apoptosis within SCOs. Results showed increased accumulation of apoptotic DNA fragments in C9-ALS SCOs, supporting the hypothesis that the *C9orf72* HRE contributes to neuronal vulnerability and cell death (Figure 2 B). Finally, MSD immunoassay was employed to quantify poly(GA) and poly(GP) levels in C9-ALS and isogenic SCOs. Immunodetection analysis revealed a marked increase of both poly(GA) and poly(GP) in C9-ALS SCOs, consistent with the characteristic molecular signatures of C9-associated ALS, further validating the SCO model as a relevant system to study DPR-related neurotoxicity (Figure 2 C).

TEM revealed clear ultrastructural differences between isogenic and C9-ALS organoids. Axonal development appeared more advanced in isogenic organoids, with elongated axons, whereas axons in C9-ALS organoids were consistently shorter. Mitochondrial morphology also differed markedly between the two groups: in C9-ALS organoids, mitochondria were often enlarged in both length and width, displaying abnormal compartmentalisation and thickened cristae, while isogenic controls contained numerous mitochondria with normal size, shape, and structural integrity. In contrast, endoplasmic reticulum (ER) morphology, including both rough (RER) and smooth (SER) components, appeared largely similar between isogenic and C9-ALS organoids, with no evident structural abnormalities observed in either group (Figure 2 D).

Single-cell transcriptomic profiling reveals multiple cellular clusters in C9-ALS SCOs

ScRNA-seq data were subjected to filtering, integration, and scaling (Supplementary Fig. 1). Despite this, transcriptomic profiles revealed a high degree of heterogeneity among samples from the three cell lines. UMAP visualisations showed incomplete overlap, indicating differences in cell distribution between conditions, suggesting that each cell line develops distinct cell clusters; in particular, cell line #2 showed a higher prevalence of neural cells, while cell line #3 exhibited a greater proportion of glial cells. Leiden clustering analysis of isogenic and C9-ALS organoids identified 10 clusters at resolution 0.5, which was found to be the most appropriate setting to delineate and distinguish different cell populations (Figure 3 A). Cell-type-specific gene sets (Supplementary Table 3), validated using data from the Human Protein Atlas (proteinatlas.org), were used to support accurate manual annotation of 8 cell populations within the SCOs (Figure 3 B). Pluripotency scores were calculated across all cells to assess the differentiation status of each population and to validate the identity of clusters. Notably, MNs, neurons, and astrocyte clusters displayed a more differentiated phenotype, whereas the undefined and vascular leptomeningeal cells (VLMCs) clusters exhibited higher pluripotency scores, indicative of a less differentiated state. Comparison of pluripotency across the two experimental conditions visualised by UMAP indicated improved differentiation in the isogenic condition (Figure 3 C). To assess the extent to which the disease model recapitulates the cellular composition of the human spinal cord and to validate the accuracy of manual cluster annotation, the expression patterns and spatial localisation of canonical neuronal and glial markers were analysed. Marker distribution confirmed cluster-specific expression profiles, consistent with expected cell type identities. Specifically, co-expression of *ChAT* and *Paired Like Homeobox 2A (PHOX2A)* delineated MN clusters, *GFAP* and *S100 Calcium Binding Protein B (S100B)* were enriched in astrocytic populations, *DCX* marked immature neurons, *Glutamate Decarboxylase 2 (GAD2)* was predominantly expressed in GABAergic neurons, *Proteolipid Protein 1 (PLP1)* and *SRY-Box Transcription Factor 10 (SOX10)* identified oligodendrocyte clusters, and *Forkhead Box J1 (FOXJ1)* was selectively expressed in ependymal cells. Additionally, one cluster could not be confidently assigned to any specific cell type based on the applied annotation criteria, preventing its definitive classification (Figure 3 D,E).

A heatmap was generated to provide an overview of marker expression patterns across all clusters (Figure 4 A). Expression analysis of cluster-specific marker genes was carried out to further support cluster annotation (Figure 4 B**,** Supplementary Table 4). Furthermore, a dot plot was generated to highlight the top five most representative genes per cluster, offering a more focused assessment of marker specificity and relative expression levels (Figure 4 C).

Transcriptional profiling identifies disease-associated signatures in C9-ALS MN and astrocyte clusters

Since MNs represent the primary neuronal subtype selectively affected in ALS, focused transcriptomic analysis of the MN cluster was performed to identify molecular alterations potentially underlying their selective vulnerability in C9-ALS. Beyond MNs, astrocytes were also analysed, given their critical role in ALS pathology through neuroinflammatory processes and impaired neuronal support (Figure 5 A).

Using the MAST algorithm, significant dysregulation of multiple genes was identified in C9-ALS MNs (Figure 5 B, Supplementary Table 5). Specifically, the MAST algorithm revealed 123 genes significantly down-regulated in C9-ALS MNs (*logFC* < −1; *FDR* < 0.05). These genes were predominantly associated with neuronal processes including neurogenesis, axonogenesis, and synapse dynamics. Additionally, 110 genes were identified as significantly up-regulated in C9-ALS MNs compared to isogenic controls (*logFC* > 1; *FDR* < 0.05). These DEGs were significantly enriched in pathways associated with RNA and ribosomal dynamics (Figure 5 C, Supplementary Table 5).

Within the astrocyte cluster, 204 genes were significantly down-regulated (*logFC* < −1; *FDR* < 0.05) in the C9-ALS condition (Figure 5 D, Supplementary Table 6). Enrichment analysis showed the down-regulation of genes involved in cell junction, and regulation of neuron projection development. Notably, cilia-related pathways were significantly down-regulated. Conversely, the MAST algorithm revealed 126 significantly up-regulated genes (*logFC* > 1; *FDR* < 0.05) mainly associated with cytoplasmic translation, ribosomal dysregulation, highlighting altered translational mechanisms (Figure 5 E, Supplementary Table 6).

Broad transcriptomic changes correlate with proteomic alterations in the affected condition

Whole-transcriptome differential expression analysis using MAST was performed across all single-cell profiles to enable cross-platform comparison between single-cell transcriptomic and MS data. In this whole-sample comparison, 131 significantly down-regulated genes were identified while 201 genes were significantly up-regulated (*logFC* thresholds > 1 and < −1, respectively; *FDR* < 0.05) (Figure 6 A, Supplementary Table 7). Down-regulated genes were enriched for pathways related to nervous system development, axonogenesis, gliogenesis, synapse organisation and assembly, whereas up-regulated pathways encompassed ribosomal activity, translation, extracellular matrix (ECM) organisation,

indicative of increased protein synthesis and altered intercellular communication (Figure 6 B, Supplementary Table 7).

MS analysis of whole SCOs was conducted to compare protein composition and abundance between C9-ALS and isogenic samples (n=3 biological replicates; n=3 technical replicates). Raw MS data obtained from each line were integrated into a single dataset for downstream analysis. To reduce variability caused by Matrigel-associated proteins from the embedding scaffold, these were filtered out. A total of 2177 proteins were retained for differential expression analysis comparing C9-ALS and control conditions. Differential proteomic analysis revealed 96 down-regulated (*logFC* < −1; *FDR* < 0.05) and 54 up-regulated (*logFC* > 1; *FDR* < 0.05) proteins in the C9-ALS condition compared to isogenic controls (Figure 6 C, Supplementary Table 8). Enrichment analysis revealed a significant down-regulation of pathways related to nervous system development, and metabolism suggesting compromised bioenergetic and metabolic function. Among the up-regulated pathways, a notable enrichment of biological processes related to RNA metabolism was observed, including mRNA processing and splicing, and nucleo-cytoplasmic transport (Figure 6 D, Supplementary Table 8).

Comparison of significantly dysregulated genes from the single-cell analysis with proteomic data revealed a subset of six terms consistently down-regulated at both the transcript and protein levels. Among these targets, NTN1 (Netrin 1), SLC1A3 (Solute Carrier Family 1 Member 3), and EFNB3 (Ephrin B3) were selected for further investigation because of their involvement in both neurodevelopmental and neurodegenerative mechanisms (Figure 6 E). Expression analysis confirmed a significant down-regulation of NTN1 at the transcript level (Figure 6 F). To further characterise NTN1 expression, we examined its distribution across different cellular populations. Transcriptomic data revealed a marked enrichment of NTN1 expression in glial cells (Figure 6 G). Notably, this result is consistent with the MAST analysis performed specifically on the astrocyte cluster, in which NTN1 was found to be significantly down-regulated in the C9-ALS condition (Figure 5 D). Western blot analysis showed no significant changes in SLC1A3 and EFNB3 in C9-ALS SCOs (data not shown). In contrast, this analysis further confirmed a significant reduction of NTN1 protein levels in the C9-ALS condition compared with isogenic controls, with similar reductions observed across all three independent cellular lines analysed (Figure 6 H). Together, these findings consistently indicate a reduction of NTN1 expression in C9-ALS, highlighting a potential astrocyte-associated alteration in NTN1 signaling.

Discussion

To investigate pathogenic events associated with C9-ALS, SCOs were generated from iPSC lines carrying the HRE in *C9orf72* and their respective isogenic controls. Overall, the temporal molecular and protein analyses indicate that both control and C9-ALS organoids undergo a progressive maturation from early neural progenitor stages toward a motor neuron–like identity over time. However, the presence of early differences in neuronal marker expression and the persistent reduction of markers associated with mature neuronal cytoskeletal organisation in C9-ALS organoids suggest a delayed and/or altered maturation trajectory (24). Importantly, despite these differences, late-stage organoids display a complex

and regionally relevant cellular composition, supporting the robustness of the differentiation protocol while highlighting disease-related alterations in neuronal development. Furthermore, increased apoptosis and DPR accumulation were observed exclusively within the affected condition, supporting the reliability of iPSC-derived SCOs for modeling key neurodevelopmental and molecular features of C9-ALS. Ultrastructural analysis by TEM supports impaired neuronal maturation, axonal degeneration, and altered mitochondrial morphology in C9-ALS organoids. The preservation of ER morphology suggests that structural alterations selectively affect specific subcellular compartments.

Single-cell profiling identified distinct cellular clusters including neuronal and glial populations. In MNs, the down-regulation of genes associated with neuronal differentiation, axonal development, and synaptic organisation suggests a disruption of core processes required for motor circuit integrity and maintenance. These changes are consistent with an impaired capacity to establish or sustain functional connectivity, a feature increasingly recognised as an early and disease-relevant hallmark of ALS pathology. Within the astrocyte cluster, a down-regulation of genes involved in cell junction organisation and the regulation of neuronal projection development suggests a reduced capacity to provide structural and trophic support to neighboring neurons. Particularly, the significant suppression of cilia-related pathways mirrors observations reported in ALS and other neurodegenerative disease models, reinforcing the emerging link between ciliary dysfunction and impaired neuro-glial signaling (25–27). Notably, the up-regulation of genes involved in RNA metabolism and ribosomal function in both MN and astrocyte clusters reflect an impairment in transcriptional and translational processes as a central pathogenic mechanism in C9-ALS (28).

Integrated multi-omics analysis identified a subset of molecular terms consistently downregulated at both the transcriptomic and proteomic levels. Notably, several of these targets are functionally linked to key neural processes. In particular, *NTN1* and *EFNB3* are implicated in pathways governing axon guidance, synaptic organization, and neuronal maintenance, with established roles in both neurodevelopment and neurodegeneration (29,30).

In parallel, *SLC1A3* emerged as a significantly downregulated target. As a major astrocytic glutamate transporter, *SLC1A3* is essential for glutamate uptake and the maintenance of excitatory neurotransmission homeostasis (31). Its reduction is consistent with impaired glutamate clearance and consequent excitotoxicity, a well-recognized pathogenic mechanism in ALS. This observation is further supported by the therapeutic rationale underlying glutamate-modulating strategies, where enhancement of transporter function has been associated with neuroprotective effects in preclinical and clinical contexts (32–36).

Our data further confirm a robust and consistent reduction of *NTN1* expression across all SCO lines, supporting its potential contribution to impaired neuronal connectivity and structural instability. Our own work and that of many others (37) has identified *NTN1* as a secreted guidance cue critically involved in axon pathfinding, neuronal migration, and circuit formation during development. Further, it regulates neuronal survival and maintenance in the adult nervous system. Beyond these canonical roles,

increasing evidence implicates *NTN1* in processes highly relevant to neurodegeneration, including the preservation of axonal integrity and the modulation of neuroinflammatory responses (29,30,38). In the context of ALS, *NTN1* has been shown to support synaptic protein homeostasis and motor neuron integrity, thereby delaying axonal degeneration, whereas its downregulation exacerbates Ubiquilin 2 (*UBQLN2*)–mediated toxicity and accelerates motor neuron loss (39). Notably, *UBQLN2*-positive aggregates represent a near-universal pathological feature in TDP-43–positive ALS, including cases associated with *C9ORF72* expansions (40), suggesting that *UBQLN2*-related mechanisms may broadly contribute to ALS pathogenesis even in the absence of causative mutations (41).

Taken together, beyond identifying a subset of candidate molecular targets, our findings demonstrate a specific and reproducible downregulation of *NTN1* in C9-ALS SCOs. This supports a model in which impaired *NTN1* signaling may contribute to disrupted neuronal connectivity and increased susceptibility to apoptosis, ultimately promoting axonal degeneration. Importantly, these molecular alterations are consistent with the ultrastructural abnormalities observed by TEM, providing convergent evidence linking *NTN1* deficiency to structural hallmarks of neurodegeneration in this system.

Conclusions

In conclusion, this comprehensive multi-omics analysis of patient-derived SCOs offers new insights into the cellular and molecular mechanisms underlying C9-ALS pathogenesis. While the organoid system successfully recapitulates key aspects of human spinal cord cytoarchitecture, it lacks vascularisation and immune cell infiltration limitations that should be considered when extrapolating these findings to the in vivo disease context. Nevertheless, by resolving disease-relevant, cell-type-specific alterations across both transcriptomic and proteomic layers including astrocyte-associated impairments in glutamate homeostasis this study establishes a robust and physiologically relevant platform for mechanistic investigation and therapeutic discovery, ultimately advancing the development of targeted interventions for ALS.

Abbreviations

amyotrophic lateral sclerosis (ALS)

motor neuron disease (MND)

familial ALS (fALS)

sporadic ALS (sALS)

spinal cord organoids (SCOs)

induced pluripotent stem cells (iPSCs)

human embryonic stem cells (hESCs)

motor neurons (MNs)

hexanucleotide repeat expansions (HREs)

chromosome 9 open reading frame 72 (C9orf72)

frontotemporal dementia (FTD)

repeat-associated non-AUG translation (RAN)

dipeptide repeat proteins (DPRs)

three-dimensional (3D)

days in vitro (DIV)

embryoid bodies (EBs)

neural induction medium (NIM)

retinoic acid (RA)

smoothened agonist (SAG)

netrin-1 (NTN1)

immunofluorescence (IF)

paraformaldehyde (PFA)

normal goat serum (NGS)

bovine serum albumin (BSA)

room temperature (RT)

phenylmethylsulfonyl fluoride (PMSF)

Meso Scale Discovery immunoassay (MSD)

transmission electron microscopy (TEM)

Electron Microscopy Sciences (EMS)

single-cell RNA sequencing (scRNA-seq)

differential gene expression (DGE)

Model-based Analysis of Single-cell Transcriptomics (MAST)

false discovery rate (FDR)

log2 fold change (logFC)

differentially expressed genes (DEGs)

Gene Ontology (GO)

biological process (BP)

mass spectrometry (MS)

variance stabilizing normalization (VSN)

western blot (WB)

standard error of the mean (SEM)

paired box 6 (PAX6)

Microtubule Associated Protein 2 (MAP2)

Choline O-acetyltransferase (ChAT)

Neurofilament Heavy Chain (NEFH)

SRY-Box Transcription factor 2 (SOX2)

ISL LIM Homeobox 1 (ISL1)

Tubulin Beta 3 Class III (TUJ1)

doublecortin (DCX)

Oligodendrocyte Transcription Factor 2 (OLIG2)

homeobox B4 (HOXB4)

peripherin (PRPH)

Glial Fibrillary Acidic Protein (GFAP)

endoplasmic reticulum (ER)

rough endoplasmic reticulum (RER)

smooth endoplasmic reticulum (SER)

vascular leptomeningeal cells (VLMCs)

Paired Like Homeobox 2A (PHOX2A)

S100 Calcium Binding Protein B (S100B)

Glutamate Decarboxylase 2 (GAD2)

Proteolipid Protein 1 (PLP1)

SRY-Box Transcription Factor 10 (SOX10)

Forkhead Box J1 (FOXJ1)

extracellular matrix (ECM)

relative fluorescence units (RFU)

quantitative PCR (qPCR)

sodium dodecyl sulfate (SDS)

bicinchoninic acid (BCA)

fluorescence-activated cell sorting (FACS)

Declarations

Data availability

All data are available in the main text or the supplementary materials. Any additional information is available from the corresponding author upon request.

Acknowledgments

The authors would like to thank Associazione Centro Dino Ferrari for its support. Computational resources have been provided by the INDACO Core facility, which is a project of High Performance Computing at the University of Milan.

Funding

This work was supported by E-Rare3 INTEGRALS (01GM1913), PRIN 2022 (PNRR-POC-2022-12375645, PRIN202223SCORT_01, PNRR_PRIN23SCORT_01), Ricerca Corrente 2026 (RC26-230-01) to SC.

Competing interests

Authors declare that they have no competing interests.

Author Contribution

M.R. and N.G. contributed equally to the main manuscript. G.G. and E.S. contributed to all bioinformatic analyses. L.B. prepared figures 1-6 and supplementary figures 1,2. M.R. and L.N. made TEM acquisitions. U.S. and T.G. made the DPR analyses. R.D. generated the repeat expansion graphics. A.M. prepared single-cell libraries. L.O., N.B., J.P., and S.C. reviewed the manuscript.

References

1. Amick J, Roczniak-Ferguson A, Ferguson SM (2016) C9orf72 binds SMCR8, localizes to lysosomes, and regulates mTORC1 signaling. Mol Biol Cell 27(20):3040–3051. 10.1091/mbc.E16-01-0003
2. Ash PE, Bieniek KF, Gendron TF, Caulfield T, Lin WL, Dejesus-Hernandez M, van Blitterswijk MM, Jansen-West K, Paul JW 3rd, Rademakers R, Boylan KB, Dickson DW, Petrucelli L (2013) Unconventional translation of C9ORF72 GGGGCC expansion generates insoluble polypeptides specific to c9FTD/ALS. Neuron 77(4):639–646. 10.1016/j.neuron.2013.02.004
3. Athieniti E, Spyrou GM (2022) A guide to multi-omics data collection and integration for translational medicine. Comput Struct Biotechnol J 21:134–149. 10.1016/j.csbj.2022.11.050
4. Babu M, Snyder M (2023) Multi-Omics Profiling for Health. Mol Cell Proteom 22(6):100561. 10.1016/j.mcpro.2023.100561. Epub 2023 Apr 27
5. Balendra R, Isaacs AM (2018) C9orf72-mediated ALS and FTD: multiple pathways to disease. Nat Rev Neurol 14(9):544–558. 10.1038/s41582-018-0047-2. PMID: 30120348; PMCID: PMC6417666
6. Brettschneider J, Van Deerlin VM, Robinson JL, Kwong L, Lee EB, Ali YO, Safren N, Monteiro MJ, Toledo JB, Elman L, McCluskey L, Irwin DJ, Grossman M, Molina-Porcel L, Lee VM-Y, Trojanowski JQ (2012) Pattern of ubiquilin pathology in ALS and FTLD indicates presence of C9orf72 hexanucleotide expansion. Acta Neuropathol 123:825–839. 10.1007/s00401-012-0970-z
7. De Decker M, Zelina P, Moens TG, Beckers J, Contardo M, Dittlau KS, Van Schoor E, Ronisz A, Eggermont K, Moisse M, Chandran S, Veldink JH, Thal DR, Van Den Bosch L, Pasterkamp RJ, Van Damme P (2025) C21ORF2 mutations point towards primary cilia dysfunction in amyotrophic lateral sclerosis. Brain 148(3):803–816. 10.1093/brain/awae331. PMID: 39703094; PMCID: PMC11884758
8. Farahani H, Ganji A, Mosayebi G, Monfared ME, Ghazavi A (2025) Netrin-1: Dual Roles in Neuroinflammation and Neurodegenerative Disease Dynamics. Int J Inflam 2025:8670048. 10.1155/ijin/8670048. PMID: 40761377; PMCID: PMC12321422
9. Faravelli I, Rinchetti P, Tambalo M, Simutin I, Mapelli L, Mancinelli S, Miotto M, Rizzuti M, D'Angelo A, Cordiglieri C, Forotti G, Peano C, Kunderfranco P, Calandriello L, Comi GP, Paraboschi E, Pali E, Beatrice F, D'Angelo E, Przedborski S, Nizzardo M, Lodato S, Corti S Targeted Antisense Oligonucleotide Treatment Rescues Developmental Alterations in Spinal Muscular Atrophy Organoids. bioRxiv. 2025.01.17.633436; 10.1101/2025.01.17.633436

10. Fumagalli E, Funicello M, Rauen T, Gobbi M, Mennini T (2008) Riluzole enhances the activity of glutamate transporters GLAST, GLT1 and EAAC1. Eur J Pharmacol 578(2–3):171–176. 10.1016/j.ejphar.2007.10.023. Epub 2007 Oct 25. PMID: 18036519
11. Gendron TF, Bieniek KF, Zhang YJ, Jansen-West K, Ash PE, Caulfield T, Daughrity L, Dunmore JH, Castanedes-Casey M, Chew J, Cosio DM, van Blitterswijk M, Lee WC, Rademakers R, Boylan KB, Dickson DW, Petrucelli L (2013) Antisense transcripts of the expanded C9ORF72 hexanucleotide repeat form nuclear RNA foci and undergo repeat-associated non-ATG translation in c9FTD/ALS. Acta Neuropathol 126(6):829–844. 10.1007/s00401-013-1192-8
12. Grad LI, Rouleau GA, Ravits J, Cashman NR (2017) Clinical Spectrum of Amyotrophic Lateral Sclerosis (ALS). Cold Spring Harb Perspect Med 7(8):a024117. 10.1101/cshperspect.a024117
13. Hardiman O, Al-Chalabi A, Chio A, Corr EM, Logroscino G, Robberecht W, Shaw PJ, Simmons Z, van den Berg LH (2017) Amyotrophic lateral sclerosis. Nat Rev Dis Primers 3:17071. 10.1038/nrdp.2017.71
14. Howland DS, Liu J, She Y, Goad B, Maragakis NJ, Kim B, Erickson J, Kulik J, DeVito L, Psaltis G, DeGennaro LJ, Cleveland DW, Rothstein JD (2002) Focal loss of the glutamate transporter EAAT2 in a transgenic rat model of SOD1 mutant-mediated amyotrophic lateral sclerosis (ALS). Proc Natl Acad Sci U S A 99(3):1604–1609. 10.1073/pnas.032539299. Epub 2002 Jan 29. PMID: 11818550; PMCID: PMC122237
15. Hulisz D (2018) Amyotrophic lateral sclerosis: disease state overview. Am J Manag Care 24(15 Suppl):S320–S326
16. Kim SH, Nichols KD, Anderson EN, Liu Y, Ramesh N, Jia W, Kuerbis CJ, Scalf M, Smith LM, Pandey UB, Tibbetts RS (2023) Axon guidance genes modulate neurotoxicity of ALS-associated UBQLN2. Elife 12:e84382 PMID: 37039476; PMCID: PMC10147378
17. Liang C, Shao Q, Zhang W, Yang M, Chang Q, Chen R, Chen JF (2019) Smcr8 deficiency disrupts axonal transport-dependent lysosomal function and promotes axonal swellings and gain of toxicity in C9ALS/FTD mouse models. Hum Mol Genet 28(23):3940–3953. 10.1093/hmg/ddz230
18. Liu Y, Wang T, Ji YJ, Johnson K, Liu H, Johnson K, Bailey S, Suk Y, Lu YN, Liu M, Wang J (2018) A C9orf72-CARM1 axis regulates lipid metabolism under glucose starvation-induced nutrient stress. Genes Dev 32(21–22):1380–1397. 10.1101/gad.315564.118
19. Maharjan N, Künzli C, Buthey K, Saxena S (2017) C9ORF72 Regulates Stress Granule Formation and Its Deficiency Impairs Stress Granule Assembly, Hypersensitizing Cells to Stress. Mol Neurobiol 54(4):3062–3077. 10.1007/s12035-016-9850-1
20. Mori K, Arzbergerv T, Grässer FA (2013) Bidirectional transcripts of the expanded C9orf72 hexanucleotide repeat are translated into aggregating dipeptide repeat proteins. Acta Neuropathol 126, 881–893 10.1007/s00401-013-1189-3
21. Nabeel Mustafa A, Salih Mahdi M, Ballal S, Chahar M, Verma R, Ali Al-Nuaimi AM, Kumar MR, Kadhim A, Al-Hussein R, Adil M, Jasem Jawad M (2025) Netrin-1: Key insights in neural development and disorders. Tissue Cell 93:102678 Epub 2024 Dec 14. PMID: 39719818

22. Nguyen L (2024) Updates on Disease Mechanisms and Therapeutics for Amyotrophic Lateral Sclerosis. Cells 13(11):888. 10.3390/cells13110888. PMID: 38891021; PMCID: PMC11172142
23. Pang W, Hu F (2021) Cellular and physiological functions of C9ORF72 and implications for ALS/FTD. J Neurochem 157(3):334–350. 10.1111/jnc.15255
24. Pajarillo E, Rizor A, Lee J, Aschner M, Lee E (2019) The role of astrocytic glutamate transporters GLT-1 and GLAST in neurological disorders: Potential targets for neurotherapeutics. Neuropharmacology 161:107559. 10.1016/j.neuropharm.2019.03.002. Epub 2019 Mar 6. PMID: 30851309; PMCID: PMC6731169
25. Qin X, Zhang X, He X, Xu H, Yao Q, Li Z, Feng Y, Zhong Y, Li Z, Lv G, Wang Y (2024) Neuron-derived Netrin-1 deficiency aggravates spinal cord injury through activating the NF-κB signaling pathway. Heliyon 10(17):e37388 PMID: 39290272; PMCID: PMC11407054
26. Rizzuti M, Sali L, Melzi V, Scarcella S, Costamagna G, Ottoboni L, Quetti L, Brambilla L, Papadimitriou D, Verde F, Ratti A, Ticozzi N, Comi GP, Corti S, Gagliardi D (2023) Genomic and transcriptomic advances in amyotrophic lateral sclerosis. Ageing Res Rev 92:102126 Epub 2023 Nov 14. PMID: 37972860
27. Rothstein JD, Van Kammen M, Levey AI, Martin LJ, Kuncl RW (1995) Selective loss of glial glutamate transporter GLT-1 in amyotrophic lateral sclerosis. Ann Neurol. ;38(1):73–84. 10.1002/ana.410380114. PMID: 7611729
28. Ryan M, Heverin M, McLaughlin RL, Hardiman O (2019) Lifetime Risk and Heritability of Amyotrophic Lateral Sclerosis. JAMA Neurol 76(11):1367–1374
29. Sala G, Beretta S, Ceresa C, Mattavelli L, Zoia C, Tremolizzo L, Ferri A, Carrì MT, Ferrarese C (2005) Impairment of glutamate transport and increased vulnerability to oxidative stress in neuroblastoma SH-SY5Y cells expressing a Cu,Zn superoxide dismutase typical of familial amyotrophic lateral sclerosis. Neurochem Int 46(3):227–234 Epub 2004 Dec 8. PMID: 15670639
30. Scarcella S, Brambilla L, Quetti L, Rizzuti M, Melzi V, Galli N, Sali L, Costamagna G, Comi GP, Corti S, Gagliardi D (2025) Unveiling amyotrophic lateral sclerosis complexity: insights from proteomics, metabolomics and microbiomics. Brain Commun 7(2):fcaf114. 10.1093/braincomms/fcaf114. PMID: 40161216; PMCID: PMC11952287
31. Selvaraj BT, Livesey MR, Zhao C et al (2018) *C9ORF72* repeat expansion causes vulnerability of motor neurons to Ca2+-permeable AMPA receptor-mediated excitotoxicity. Nat Commun 9:347. 10.1038/s41467-017-02729-0
32. Serpieri V, D'Abrusco F, Valente EM (2025) The relevance of primary cilia in neurological disorders. Lancet Neurol. Jul 21:S1474-4422(25)00226-1. 10.1016/S1474-4422(25)00226-1. Epub ahead of print. PMID: 40706604
33. Sivadasan R, Hornburg D, Drepper C, Frank N, Jablonka S, Hansel A, Lojewski X, Sterneckert J, Hermann A, Shaw PJ, Ince PG, Mann M, Meissner F, Sendtner M (2016) C9ORF72 interaction with cofilin modulates actin dynamics in motor neurons. Nat Neurosci 19(12):1610–1618. 10.1038/nn.4407

34. Sullivan PM, Zhou X, Robins AM, Paushter DH, Kim D, Smolka MB, Hu F (2016) The ALS/FTLD associated protein C9orf72 associates with SMCR8 and WDR41 to regulate the autophagy-lysosome pathway. Acta Neuropathol Commun 4(1):51. 10.1186/s40478-016-0324-5
35. Tong J, Huang C, Bi F, Wu Q, Huang B, Liu X, Li F, Zhou H, Xia XG (2013) Expression of ALS-linked TDP-43 mutant in astrocytes causes non-cell-autonomous motor neuron death in rats. EMBO J 32(13):1917–1926. 10.1038/emboj.2013.122. Epub 2013 May 28. PMID: 23714777; PMCID: PMC3981181
36. Traag VA, Waltman L, van Eck NJ (2019) From Louvain to Leiden: guaranteeing well-connected communities. Sci Rep 9:5233. doi.org/10.1038/s41598-019-41695-z
37. van Battum EY, van den Munkhof MH, Pasterkamp RJ (2025) Novel insights into the regulation of neuron migration by axon guidance proteins. Curr Opin Neurobiol 92:103012. https://doi.org/10.1016/j.conb.2025.103012
38. van der Geest AT, Jakobs CE, Ljubikj T, Huffels CFM, Cañizares Luna M, Vieira de Sá R, Adolfs Y, de Wit M, Rutten DH, Kaal M, Zwartkruis MM, Carcolé M, Groen EJN, Hol EM, Basak O, Isaacs AM, Westeneng HJ, van den Berg LH, Veldink JH, Schlegel DK, Pasterkamp RJ (2024) Molecular pathology, developmental changes and synaptic dysfunction in (pre-) symptomatic human C9ORF72-ALS/FTD cerebral organoids. Acta Neuropathol Commun 12(1):152. 10.1186/s40478-024-01857-1. PMID: 39289761; PMCID: PMC11409520
39. Volos P, Fujise K, Rafiq NM (2025) Roles for primary cilia in synapses and neurological disorders. Trends Cell Biol 35(1):6–10. 10.1016/j.tcb.2024.10.014. Epub 2024 Nov 25. PMID: 39592366
40. Wolf F, Angerer P, Theis F (2018) SCANPY: large-scale single-cell gene expression data analysis. Genome Biol 19:15. 10.1186/s13059-017-1382-0
41. Yuasa-Kawada J, Kinoshita-Kawada M, Hiramoto M, Yamagishi S, Mishima T, Yasunaga S, Tsuboi Y, Hattori N, Wu JY (2025) Neuronal guidance signaling in neurodegenerative diseases: Key regulators that function at neuron-glia and neuroimmune interfaces. Neural Regen Res 21(2):612–635. 10.4103/NRR.NRR-D-24-01330. Epub 2025 Feb 24. PMID: 39995079; PMCID: PMC12220729

Figures

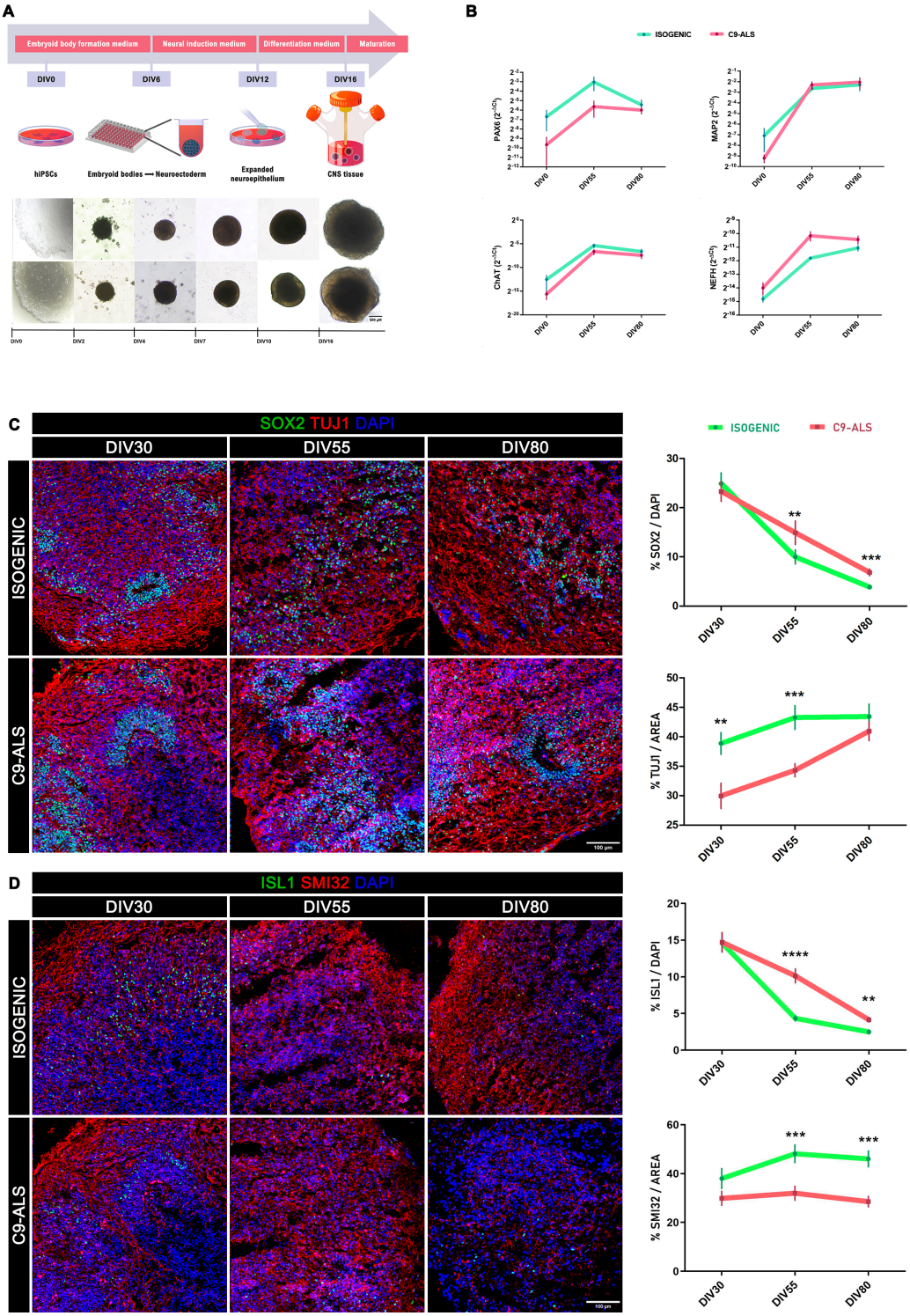


Figure 1

Generation and characterisation of isogenic and C9-ALS SCOs. (A) Schematic representation of SCO differentiation protocol and timeline with representative brightfield images at indicated time points (4X magnification). **(B)** qPCR analysis of *PAX6*, *MAP2*, *ChAT*, and *NEFH* in isogenic and C9-ALS organoids at DIV0, DIV55, and DIV80. Data are expressed as fold change relative to *GAPDH* (mean ± SEM; n=3) using the $2^{-\Delta Ct}$ method. **(C)** Representative images of SCOs stained for SOX2, TUJ1, and DAPI (nuclei) at

DIV30, DIV55 and DIV80, with relevant quantification expressed in percentage (***$p < 0.001$, **$p < 0.01$). Scale bar = 100 µm. **(D)** Representative images of SCOs stained for ISL1, SMI32, and DAPI (nuclei) at DIV30, DIV55 and DIV80, with relevant quantification expressed in percentage (****$p < 0.0001$, ***$p < 0.001$, **$p < 0.01$). Scale bar = 100 µm.

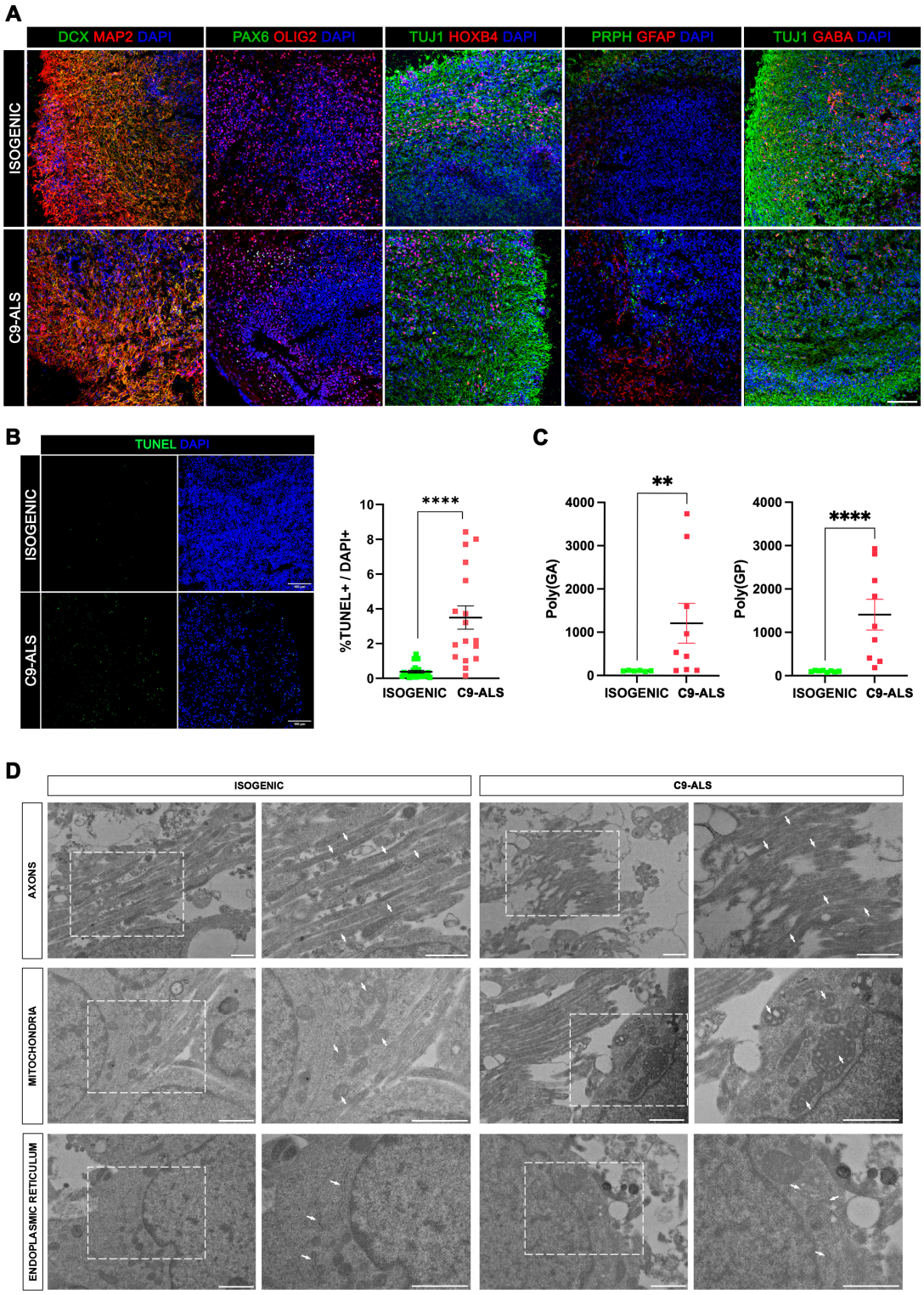


Figure 2

Analysis of spinal cord-like features and C9-linked phenotypes in iPSC-derived SCOs. **(A)**Representative IF images of DIV80 SCOs stained for DCX/MAP2, PAX6/OLIG2, TUJ1/HOXB4, PRPH/GFAP, and TUJ1/GABA. Nuclei were counterstained with DAPI (blue). Scale bar **=** 100 µm. **(B)** Representative images of TUNEL assay in isogenic and C9-ALS DIV80 SCOs with quantification of TUNEL-positive cells relative to DAPI+ nuclei expressed in percentage (%; mean ± SEM). ****p< 0.0001, unpaired Student's *t*-test. Scale bar = 100 µm. **(C)**Quantification of poly(GA) and poly(GP) DPR levels by MSD immunoassay (mean ± SEM). **p < 0.01, ****p < 0.0001, unpaired Student's *t*-test. **(D)** Representative TEM images showing axons, mitochondria, and endoplasmic reticulum in isogenic control and C9-ALS organoids. Dashed boxes highlight regions of interest that are shown at higher magnification in the right panels for each condition; white arrows indicate the selected subcellular structures. Scale bar = 1 µm.

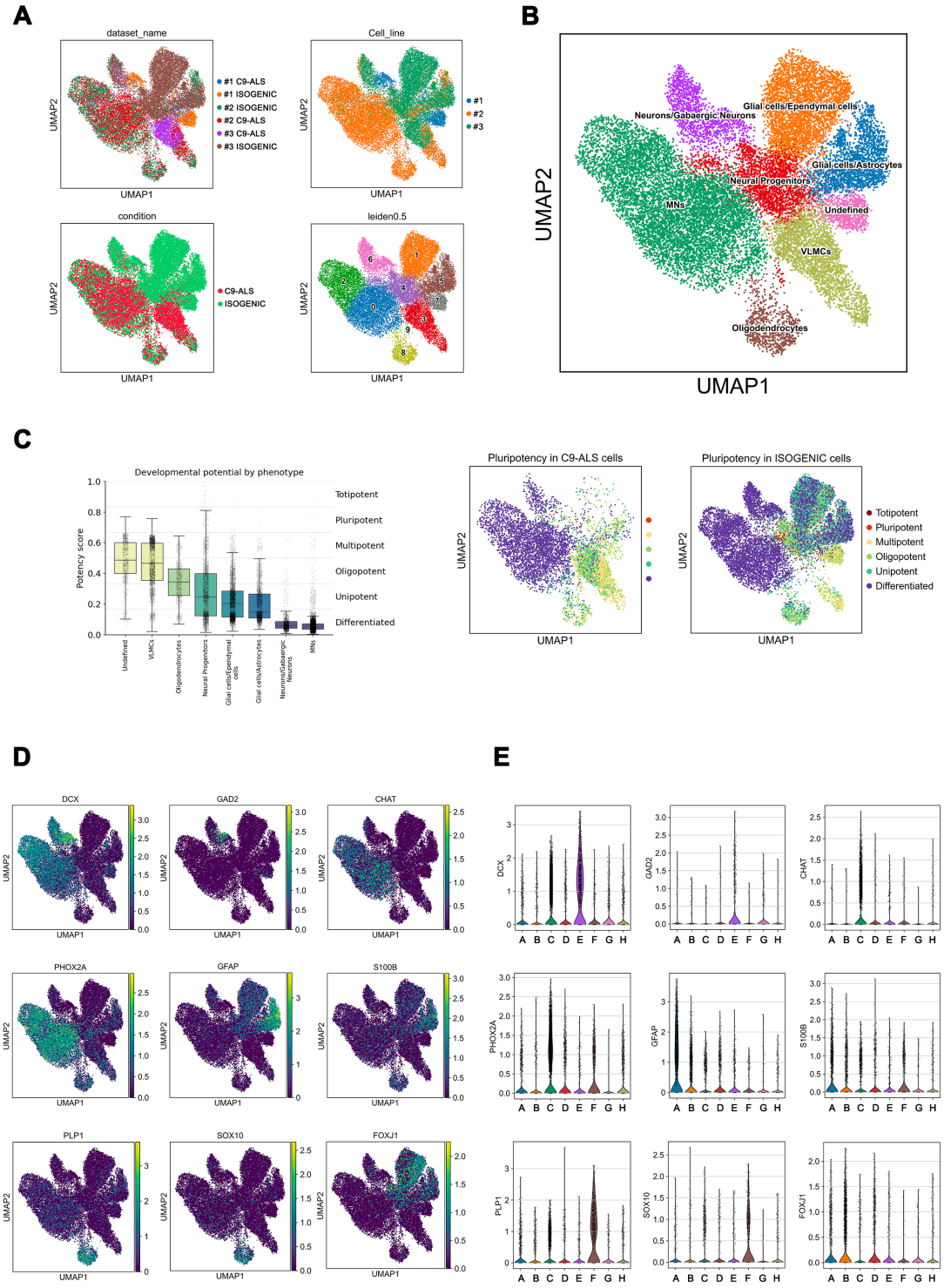
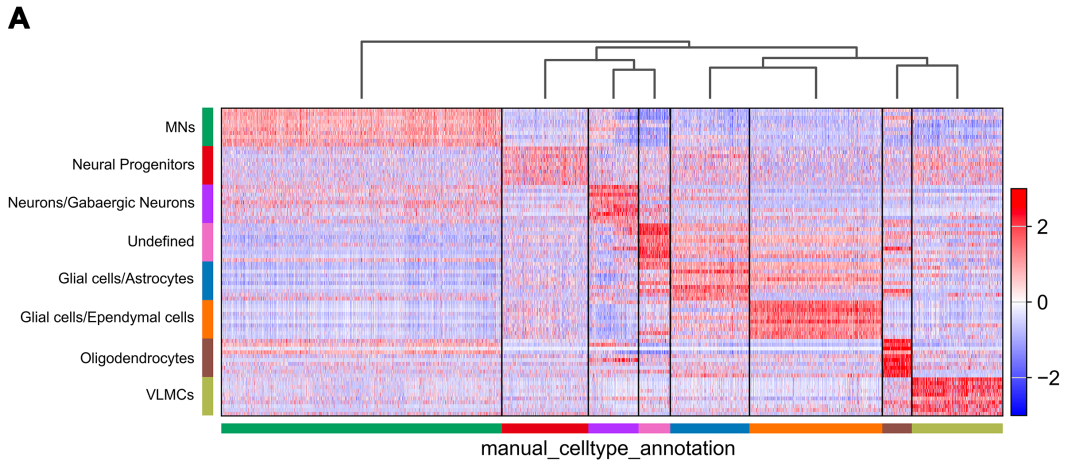
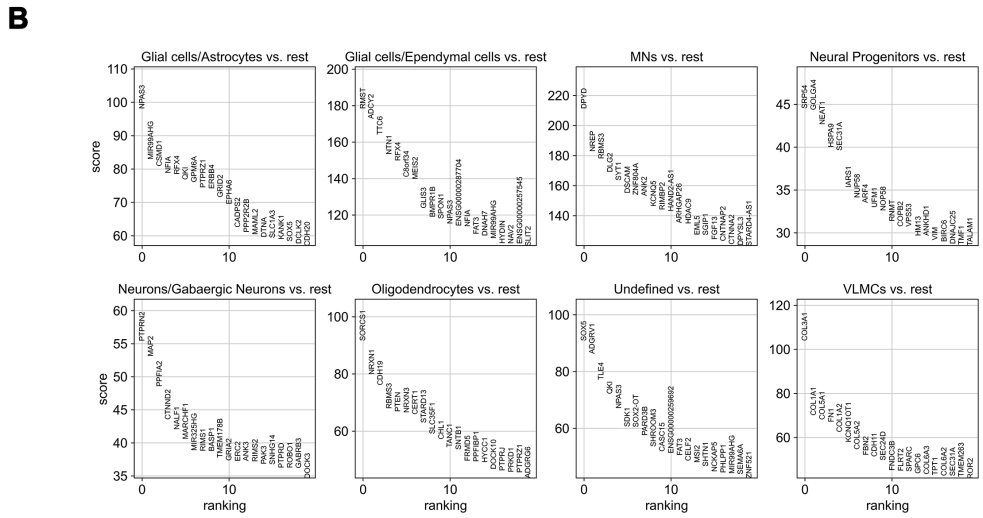


Figure 3

ScRNA-seq analysis of iPSC-derived SCOs. (**A**) UMAP plots showing the distribution of cells according to sample, cell line, experimental condition, and clusters identified using the Leiden clustering algorithm with a resolution of 0.5. **(B)** UMAP plot showing the manually annotated clusters: glial cells/astrocytes, glial cells/ependymal cells, MNs, neuronal progenitors, neurons/GABAergic neurons, oligodendrocytes, undefined cell cluster, and VLMCs. **(C)** Box plot of CytoTRACE potency scores showing developmental

potential by cell population, and UMAP plots of isogenic and C9-ALS cells colored by pluripotency score. **(D)** UMAP plots illustrating the expression of lineage-specific markers: DCX (neurons), GAD2 (GABAergic neurons), ChAT and PHOX2A (MNs), GFAP and S100B (astrocytes), PLP1 and SOX10 (oligodendrocytes), and FOXJ1 (ependymal cells). **(E)** Violin plots showing the expression of lineage-specific markers across clusters. A: glial cells/astrocytes, B: glial cells/ependymal cells, C: MNs, D: neural progenitors, E: neurons/GABAergic neurons, F: oligodendrocytes, G: undefined cell cluster, H: VLMCs.





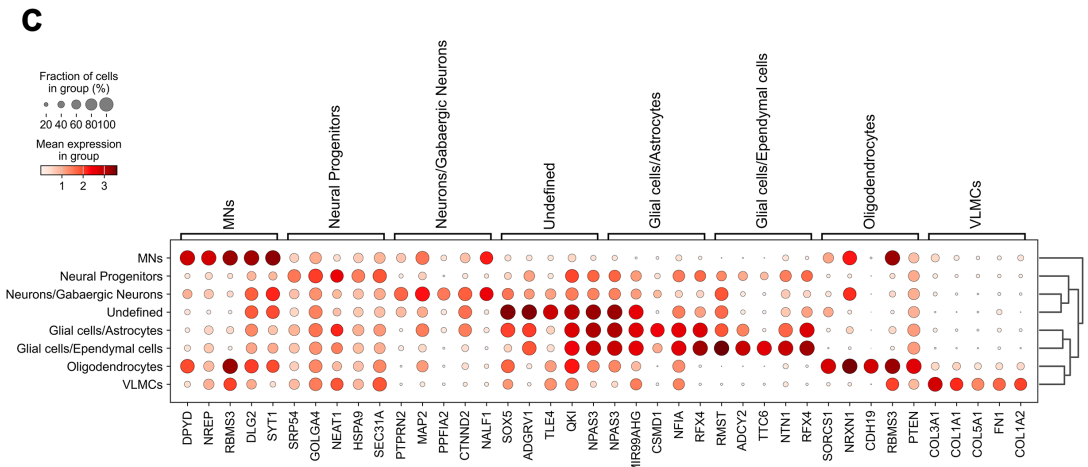


Figure 4

Identification of cluster-specific markers in scRNA-seq analysis. (A) Heatmap showing the expression of cluster-specific marker genes with hierarchical clustering of cell populations. Color scale indicates *z*-scored expression (red: high, blue: low). **(B)** Ranking plots of specific markers across identified cell clusters. Plots display top-ranked genes identified using the *t*-test method. **(C)** Dot plot showing the expression of the top 5 marker genes per cluster with hierarchical clustering of cell population. Dot size indicates fraction of cells expressing each gene; color intensity indicates mean expression level.

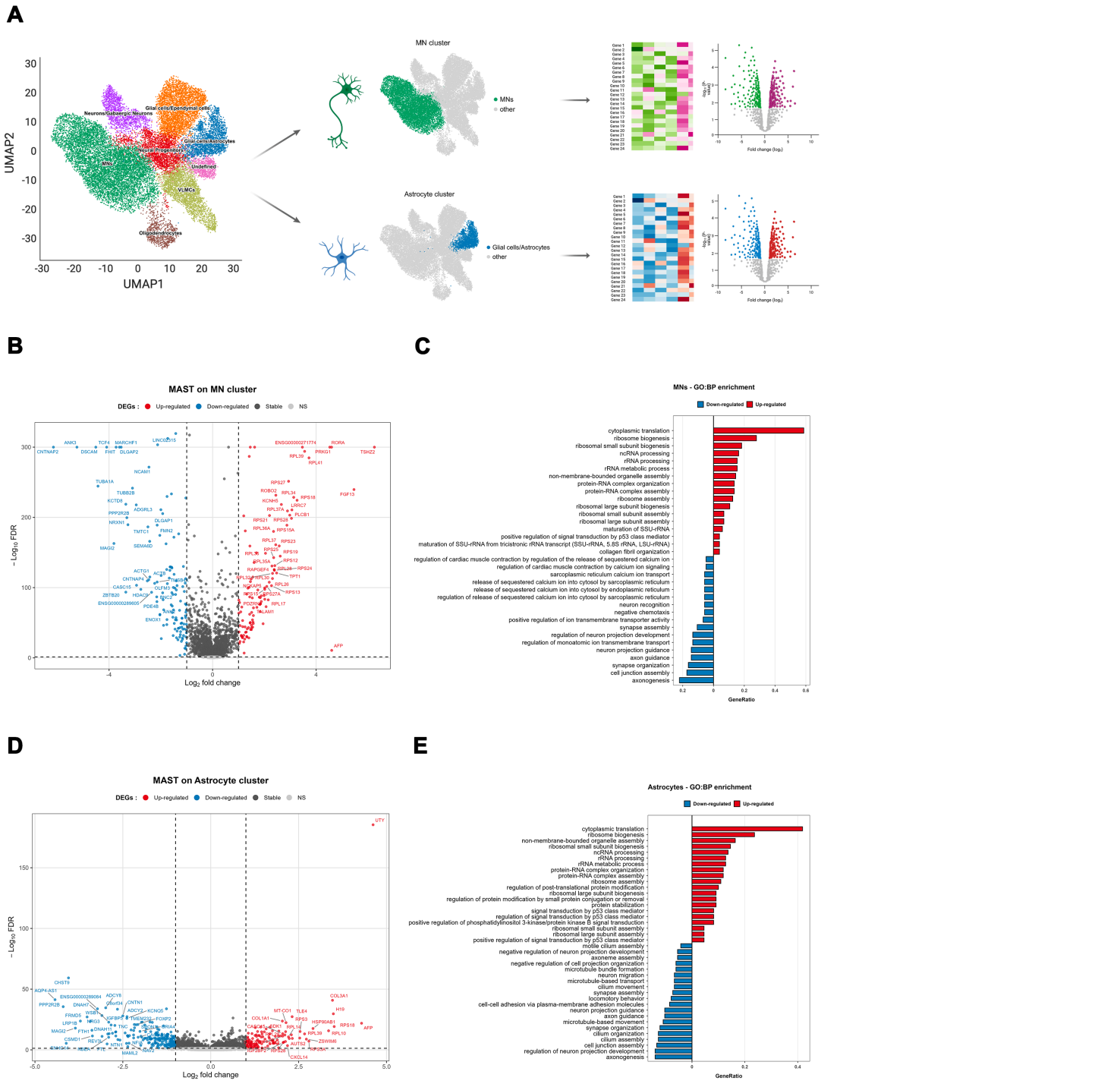


Figure 5

ScRNA-seq differential expression analysis in MN and astrocyte clusters. (A) Schematic overview of differential expression analysis workflow for MN and astrocyte clusters. **(B)** Volcano plot showing DEGs in the MN cluster (C9-ALS vs isogenic). Significance threshold: *FDR*< 0.05. Red dots: up-regulated genes (*logFC* > 1); blue dots: down-regulated genes (*logFC* < −1); gray dots: stable and non-significant. **(C)** GO:BP enrichment analysis of DEGs identified by MAST within the MN cluster. Bars represent the top

enriched GO terms ranked by adjusted *p*-value, with gene ratios shown on the x-axis. GeneRatio indicates the proportion of input genes associated with each GO term relative to the total number of input genes that were successfully mapped to GO terms in the BP ontology. **(D)**Volcano plot showing DEGs in the astrocyte cluster (C9-ALS vs isogenic; *FDR*< 0.05, |*logFC*| > 1). **(E)** GO:BP enrichment analysis showing the top enriched GO terms ranked by adjusted *p*-value, with gene ratios shown on the x-axis, associated with significant DEGs identified by MAST within the astrocyte cluster.

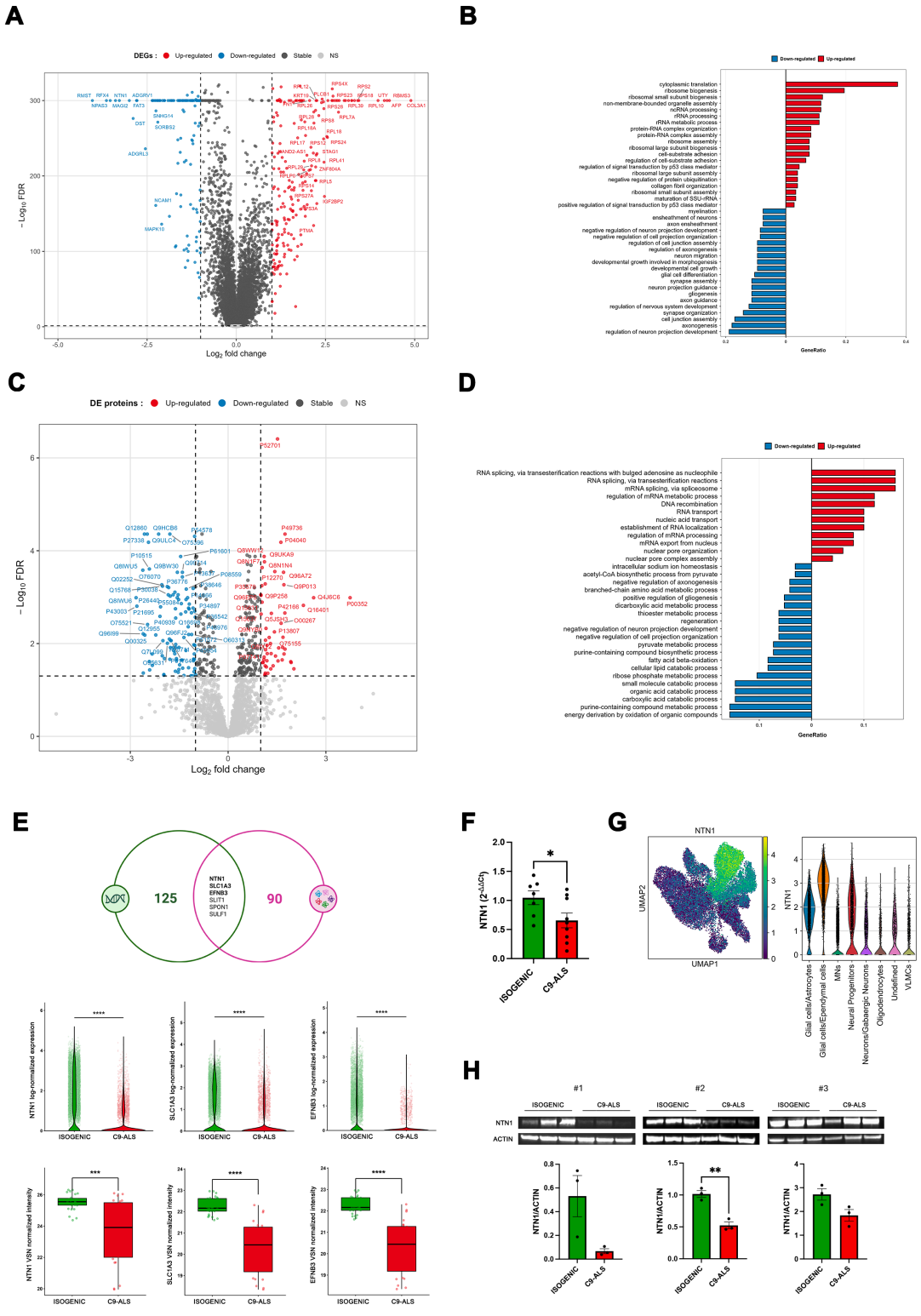


Figure 6

Integrated transcriptomic and proteomic profiling identifies convergent dysregulated targets. (A) Volcano plot showing DEGs (C9-ALS vs isogenic) identified by MAST across all cells. Red dots: up-regulated genes (*logFC* > 1; *FDR* < 0.05); blue dots: down-regulated genes (*logFC* < −1; *FDR* < 0.05); gray dots: stable and non-significant genes. **(B)** GO:BP enrichment analysis of DEGs. Enrichment was performed separately for up-regulated and down-regulated genes identified by MAST across all cells (*FDR* < 0.05, |*logFC*| > 1). Bars represent the top enriched GO terms ranked by adjusted *p*-value, with gene ratios shown on the x-axis. Enrichment significance was assessed using Benjamini–Hochberg–adjusted *p*-values. GeneRatio indicates the proportion of input genes associated with each GO term relative to the total number of input genes that were successfully mapped to GO terms in the BP ontology. **(C)** Volcano plot showing DE proteins (C9-ALS vs isogenic). Red dots: up-regulated proteins (*logFC* > 1; *FDR* < 0.05); blue dots: down-regulated proteins (*logFC* < −1; *FDR* < 0.05); gray dots: stable and non-significant proteins. **(D)** GO:BP enrichment analysis of DEGs corresponding to differentially expressed proteins from MS analysis. Enrichment was performed separately for up-regulated and down-regulated terms (*FDR* < 0.05, |*logFC*| > 1). Redundant GO terms were removed using the simplify function (cutoff = 0.7, by adjusted *p*-value) before selecting the top enriched terms. **(E)** Overlapping data from transcriptomic and proteomic results. The Venn diagram shows 125 genes (green) uniquely dysregulated at RNA level and 90 proteins (red) uniquely dysregulated. Six targets were consistently dysregulated at both levels. Among them, NTN1, SLC1A3, and EFNB3 violin plots show scRNA-seq data, with expression values normalised and differential expression assessed using MAST (******** *FDR* < 0.0001). Box plots show corresponding proteomic data (normalised counts), with statistical significance evaluated using the Wilcoxon test (******* $p < 0.001$; ******** $p < 0.0001$). **(F)** qPCR analysis of NTN1 expression across conditions. Data are expressed as fold change relative to *GAPDH* (mean ± SEM; n=3) using the $2^{-\Delta\Delta Ct}$ method. **(G)** UMAP visualisation and violin plots illustrating NTN1 expression across distinct cellular populations. **(H)** WB and densitometric analysis of NTN1 in #1, #2, #3 cell lines in C9-ALS condition compared to the respective isogenic control (** $p < 0.01$, unpaired Student's *t*-test).

Supplementary Files

This is a list of supplementary files associated with this preprint. Click to download.

- Graphicalabstract.jpeg
- FigureS1.png
- FigureS2.png
- TableS1.pdf
- TableS2.pdf
- TableS3.pdf
- TableS4.pdf

- TableS5.pdf
- TableS6.pdf
- TableS7.pdf
- TableS8.pdf